Contents lists available at ScienceDirect

Combustion and Flame

journal homepage: www.sciencedirect.com/journal/combustion-and-flame





An experimental platform for semi-autonomous kinetic model refinement combining optimal experimental design, computer-controlled experiments, and optimization leads to new understanding of $N_2O + O$

Mark C. Barbet ^a, Joe Lee ^a, Carly E. LaGrotta ^a, Rodger E. Cornell ^{a,b}, Michael P. Burke ^{a,c,d,*}

- ^a Department of Mechanical Engineering, Columbia University, New York, NY, 10027, USA
- b U.S. Army DEVCOM Army Research Laboratory, Weapon Propulsion Sciences Branch, Aberdeen Proving Ground, MD, 21005, USA
- ^c Department of Chemical Engineering, Columbia University, New York, NY, 10027, USA
- ^d Data Science Institute, Columbia University, New York, NY, 10027, USA

ARTICLE INFO

Keywords: Experiment design Automated experiments Nitrogen kinetics Uncertainty quantification N_2O decomposition

ABSTRACT

Automated platforms could enable the unprecedented pace required for modeling the countless proposed alternative fuels relevant to future technologies, but existing platforms rely exclusively on automatically generated computational data and lack experimental validation. Here, we introduce an experimental platform for rapid kinetic model refinement that combines optimal experimental design, computer-controlled experiments, and optimization-each of which are tailored in novel ways to form a cohesive platform together. The optimal experimental design considers (1) realistic uncertainties in both experimental conditions and measurements and (2) diverse reactant mixtures that can include "chemical sensitizers," which are not necessarily reactants in a specified Quantity of Interest (QoI) but sensitize kinetic information relevant to a QoI. Similarly, our High-Throughput Jet-Stirred Reactor (HT-JSR) features (1) rapid multi-species diagnostics that can measure dozens of species within minutes, (2) a flow delivery system that can prepare up to ~10-component reactant mixtures, and (3) computer-controlled operation of all components. Finally, a postprocessing code automatically retrieves data from the instruments, quantifies uncertainties in both experimental conditions and measurements, and produces self-contained files usable for optimization in our MultiScale Informatics software. This platform is demonstrated for the rate constant for $N_2O + O \Rightarrow N_2 + O_2$ as the QoI where, unlike for N₂O + O

NO + NO, proposed values at ~1000 K span ~5 orders of magnitude yet give equally good agreement with previous experimental data—suggesting that previous experiments fail to constrain the branching ratio of N₂O + O. The results show that optimal conditions with more species as both reactants and analytes—particularly NO₂ as both a reactant and analyte—enable unambiguous discrimination of the main products of N_2O + O. Specifically, the data preclude N_2 + O_2 as the main products at ${\sim}1000$ K-contrary to most recently proposed values.

Novelty and significance statement

We introduce a novel experimental platform for rapid kinetic model refinement that combines optimal design, computer-controlled experiments, and optimization—each uniquely tailored to form a cohesive platform. It notably employs high levels of automation, high-throughput multi-species diagnostics, and uniquely diverse reactant mixtures to accelerate scientific discovery. This platform is shown to achieve a goal that no previous experiment has: decipher the main products of N_2O+O . This success—attributable to the platform's unique design principles—demonstrates the effectiveness of this experimental platform as a tool for accelerating scientific discovery and kinetic model development.

^{*} Corresponding author at: Department of Mechanical Engineering, Columbia University, New York, NY, 10027, USA. E-mail address: mpburke@columbia.edu (M.P. Burke).

1. Introduction

In the year 2021, approximately 85% of the world energy supply originated from the combustion of fuels [1], and it is estimated that combustion will remain a key part of the world energy mix well into the 21st century [2,3]. However, to address pressing needs for the future energy landscape, next-generation combustion technologies will need to be more fuel-efficient, produce less emissions, and operate on non-traditional (carbon-neutral) fuels [4,5]. Furthermore, these technological improvements must be accomplished on the rapid timescales necessary to address these societal issues in an effective manner.

Predictive engine simulations provide a promising means of accelerating engine development [6–10], but they depend on having accurate kinetic models for fuel oxidation. Given the ever-expanding landscape of potential 21st century fuels, such models are consequently required for a wide range of potential fuels, many of which have been scarcely characterized, on the rapid timescales necessary.

Such rapid timescales present a significant challenge to the current paradigm for developing reliable kinetic models. Namely, the most accurate and comprehensive models often result from the combined efforts of modelers, theoreticians, and experimentalists spanning many decades (e.g., for n-heptane [11–14]). Automated model construction [15–18] can conceivably speed up model development, but any initial model (whether created by a human or a computer) generally undergoes rigorous refinement to be sufficiently reliable for predictive simulation.

That is, the model, once created, undergoes a repeated process of selecting what data are useful, generating such data experimentally or computationally, and integrating these data into improved models. While each of these tasks has traditionally required time-intensive effort, there are, or may soon be, techniques that automate these tasks. For example, optimal experimental design [19–23] automates data selection (to best inform predictions of some Quantity of Interest, QoI), automated theoretical kinetics calculations [24–27] automates computational data generation, and inverse uncertainty quantification (UQ) [28–32] automates data integration into improved models. Linking these existing tools together and with emerging automated experimental apparatuses [33,34], in principle, would create an automated platform for rapid kinetic model development and validation [32].

Two recent studies [35,36] take advantage of automated theoretical kinetics calculations to create platforms for autonomous kinetic model refinement based on optimally selected computational data. While such computational platforms can accelerate model refinement, experimental validation and training is instrumental to the development of predictive models [31,37] and would likewise be an essential component of any rapid model development pipeline.

To this end, we present a platform for rapid kinetic model refinement and validation that involves selection, generation, and integration of *experimental* data. Specifically, this platform consists of an algorithm for optimal experimental design, a computer-controlled experimental facility, a code to retrieve and post-process the experimental data, and inverse UQ to integrate the experimental data into improved models. Notably, each of the elements were designed in concert to form a cohesive platform—motivating many novel aspects of each element.

For example, the optimal experimental design approach considers realistic limitations and uncertainties for the experimental apparatus. This approach uniquely considers uncertainties in the experimental conditions to avoid selection of experiments whose interpretations are heavily influenced by uncertainties in the nominal conditions. Additionally, the measurement uncertainties include both percent reading (e.g., 10% of the measured value) and minimum (e.g., 10 ppm) error contributions to avoid selection of experiments whose information content relies on measurements near or below the instrument detection limits.

The experimental apparatus was designed with optimal design and automation in mind, intended to achieve high information generation rate with minimal human intervention. It uses a jet-stirred reactor, which can operate continuously, change conditions relatively quickly, measure many chemical species, and explore both low- and high-temperature combustion regimes. Our high-throughput jet-stirred reactor (HT-JSR) facility also has several key attributes.

First, the flow delivery system enables reactant mixture preparation of up to ten reactants. These many-component reactants could then include both the reactants in a QoI (e.g., fuel and oxidizer) and "chemical sensitizers"—species that are not reactants in the QoI but may accentuate kinetics important to predicting the QoI. This notion is inspired by kinetic "perturbation" studies [38] where species, chosen by chemical intuition/creativity and/or sensitivity analysis, were added to sensitize specific reactions [38–42]. Here, the consideration of many-component reactants enables the optimal design algorithm to be "creative" in identifying effective chemical sensitizers. For example, earlier optimal design results identified that adding CH₄ to atmospheric-pressure dimethyl ether oxidation experiments accentuates abstraction reactions by CH₃ important to predicting high-pressure ignition delays [43]. Altogether, the ability to choose and prepare complex many-component mixtures allows for high information content per datum.

Second, the array of multi-species diagnostics can measure many dozens of species within minutes. These fast, multi-species diagnostics allow for high data generation rate, particularly when combined with the following feature.

Third, all components of experimental operation and diagnostic measurements are computer controlled (and automatable). Our new post-processing code retrieves the data directly from the instruments and produces structured data files for inverse UQ. This code thereby enables (1) automation of the most time-consuming part of our experimentation, (2) rigorous UQ in a tractable manner, and (3) complete cataloging of meta-data and data analysis procedures. Furthermore, the combination of automated pre- and post-experimental procedures (i.e., optimal design and data post-processing) enables the real-time coupling with computations widely envisioned as the next frontier of science in the data age [44].

This platform for selection, generation, and integration of new experimental data is demonstrated here for the N₂O mechanism

$$N_2O(+M) \rightleftharpoons N_2 + O(+M)$$
 (R1)

$$N_2O + O \rightleftharpoons N_2 + O_2 \tag{R2}$$

$$N_2O + O \rightleftharpoons NO + NO \tag{R3}$$

whose characterization remains a significant challenge despite its apparent simplicity and importance to many applications (e.g., NO_x formation [45,46], NH_3 /biomass combustion [47,48], energetic materials [49,50]). Of the N_2O + O reactions (R2) and (R3), the rate constant for (R3) is relatively well established [51,52]. However, the rate constant of (R2) has been subject to more debate [53].

Unlike (R3) whose reverse rate constant can also be measured, experimental determinations of k_2 have generally relied on interpretations of N₂O decomposition experiments. The original interpretations of these experiments [54–56] yielded k_2 that, at low to intermediate temperatures, suggest N₂ + O₂ are the main products of N₂O + O (i.e., $k_2/k_3 \gg 1$). However, as shown in our companion paper [53], the same experimental data can also be reproduced equally well using *much lower* k_2 (~10⁴ times lower at 1000 K) and suggest NO + NO are the main products (i.e., $k_2/k_3 \ll 1$). The fact that previous experimental data therefore fail to constrain k_2 (or even decipher the main products of N₂O + O) makes this system an interesting test case for the experimental platform introduced here.

In the sections below, we describe the key elements of our platform for selection, generation, and integration of new experimental data. We then show that this platform can achieve a goal that no previous experiment over the past several decades appears to have done: decipher the

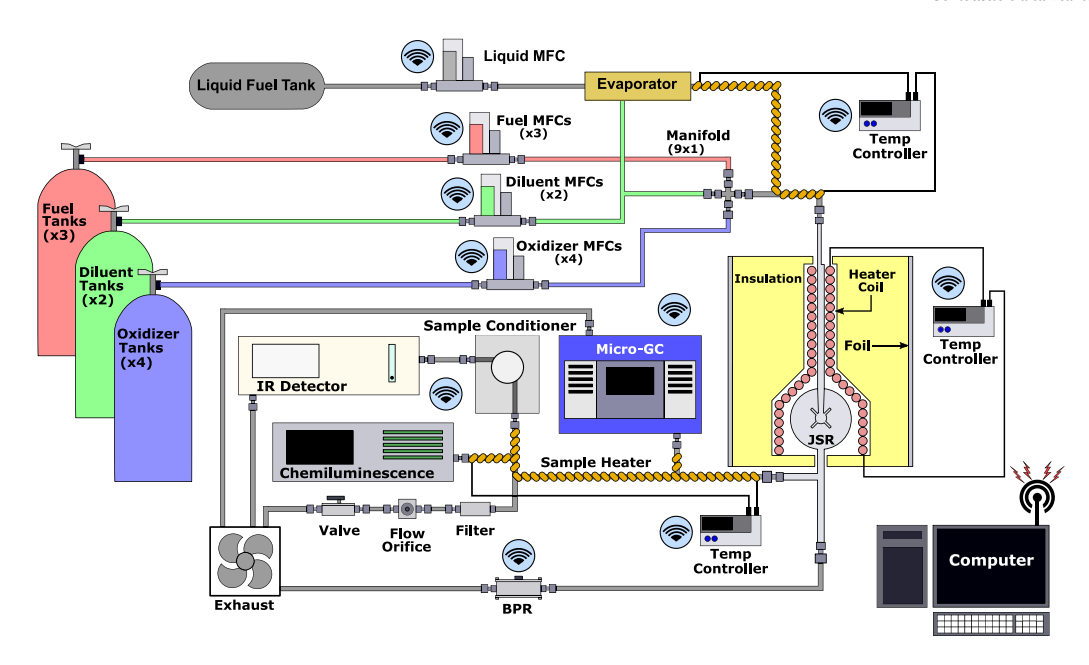


Fig. 1. The layout of the experimental equipment to be used in this platform. "Wireless" symbols indicate devices that are controllable via the networked computer and therefore available for automation.

main products of N_2O+O . Finally, we present analyses that indicate that this success can be attributed, in large part, to the present inclusion of NO_2 as a reactant and analyte—neither of which were included in previous experimental studies and both of which are consistent with the unique design principles of our platform (many-component reactants and many-species diagnostics)—altogether implying that this platform is likely to be a key tool in accelerating scientific discovery and kinetic model development.

2. Methods

The platform for selection, generation, and integration of experimental data is presented below, beginning with the experimental apparatus (for data generation), to which the optimal design (for data selection) and inverse UQ approach (for data integration), discussed thereafter, are tailored. Then, the details of its implementation to decipher the main products of the N_2O+O reaction are presented.

2.1. Computer-controlled apparatus for experimental data generation

The HT-JSR facility at Columbia University (Fig. 1), first used by Cornell et al. [57], was designed with automation and optimal experimental design in mind. This facility features: (1) a flow delivery system that can prepare reactant mixtures of up to 10 components, (2) diagnostics that measure a diverse list of stable chemical species in under five minutes, and (3) computer-controllable components.

The flow delivery system utilizes nine Bronkhorst thermal mass flow controllers (MFCs) for metering gases and a Bronkhorst (CORI-FLOW) Coriolis mass flow controller (in conjunction with an evaporator) for metering and vaporizing liquids. The gases are then combined in a mixing manifold just upstream of the JSR to prepare the gaseous reactant mixture.

The JSR, manufactured from fused silica, is based on the design by Herbinet et al. [58–60] following standard design rules [61,62]. This reactor design, in particular, has been found to closely approximate a perfectly stirred reactor under its designed range of conditions [63,64] and has been used extensively for kinetic studies [57–60,65,66]. Prior to its entry to the JSR, the gaseous reactant mixture from the mixing manifold flows through a thin, annular pre-heat zone with low residence time and large surface area where it is rapidly heated

to improve thermal homogeneity in the reactor [67]. Subsequently, the pre-heated gaseous reactant mixture flows into the $\sim\!56\text{-mm-inner-diameter}$ spherical reactor (with internal volume of 82 ± 2 cm³ [57]) via four $\sim\!0.25\text{-mm-inner-diameter}$ nozzles oriented in a crossed configuration angled $\sim\!45^\circ$ from the equatorial plane to promote turbulent mixing and high recycling rates. Overall, considering uncertainties in the reactor volume and typical uncertainties in reactant flow rates, nominal residence times in the reactor can generally be controlled to within $\pm5\%$ accuracy.

The reactor temperature is controlled with a Thermocoax heating element coiled around the reactor and pre-heat zone, both of which are wrapped in ceramic insulation. This insulated heater allows the system to reach temperatures just above 1200 K, within an uncertainty of $\pm 1\%$ (accounting for contributions due to both measurement uncertainty and spatial non-homogeneity [57]). The system achieves steady-state after a change in the temperature setpoint within $\sim\!\!10$ min—such that the experimental temperature can be varied relatively quickly.

After the reactor, flow splits in two directions: (1) an exhaust line with a PID-controlled back-pressure regulator and (2) a heated sample line towards the diagnostic equipment. The experimental pressure is maintained at 1.02 atm with better than 1% uncertainty [57]. To minimize wall reactions in the sample line, the stainless steel tubes have been coated with a SilcoNert coating, an inert non-reactive silica coating. Condensation of low-volatility mixture components is avoided through the use of a resistive heater wrapped around the coated tubes to maintain a temperature of ~385 K.

Three online, rapid-throughput diagnostics draw from the sample line: (1) a four-column Inficon Fusion micro gas chromatograph (GC), which can measure mole fractions for a wide array of common combustion products with typical measurement times under 3 min, (2) an Eco Physics AG nCLD 844 CMhr chemiluminescence analyzer (CLA), which can measure real-time mole fractions of NO, NO $_{\rm x}$, and NO $_{\rm x}$ /amines in the general range of 25 ppb to ~500 ppm (with the max depending somewhat on the mixture conditions, e.g., see [57,65]), and (3) Infrared Industries IR 208 gas analyzers containing four infrared (IR) channels, which can measure real-time mole fractions of NO, NO $_{\rm 2}$, N $_{\rm 2}$ O, and NH $_{\rm 3}$ at various ranges, and an electrochemical cell (ECC), which can measure real-time mole fractions of NO up to 5000 ppm. All of these diagnostics are controllable from a remote PC via API tools, enabling automated operation and data retrieval.

2.2. Optimal design for experiment selection

Automated experiment selection uses the established paradigm of model-based optimal design [19-23], where a set of possible experiments are simulated using a model based on prior knowledge and then experiments are selected to minimize the Shannon entropy of a model or uncertainty in a QoI (e.g., a specific rate constant, flame speed, or ignition delay time). While highly sophisticated methods can choose an optimal set of experiments [20] or consider nonlinear responses of predictions to model inputs [19], the present work uses a simple method (similar to [23]) that assumes a linear response of simulated experimental observables to model inputs and chooses the best experiments one at a time. The main innovations here involve: (1) consideration of uncertainties in the experimental conditions (leveraging the unique capabilities of the MultiScale Informatics (MSI) approach [32,68,69] employed); (2) fidelity of experimental capabilities and uncertainties to an actual apparatus (leveraging our in-house knowledge of our experiment); and (3) consideration of many-component mixtures (leveraging our unique experimental setup and the notion of "chemical sensitizers" inspired by kinetic perturbation studies [38-42]).

Before optimal (future) experiments are selected, an uncertainty-quantified model, whose uncertainties are constrained by prior (existing) data, is created. Here, this is accomplished using our MSI approach. Like many other inverse UQ procedures [23,30,31], MSI seeks to optimize and quantify uncertainties for a set of active model parameters, x, based on a set of target data, y^t , via minimization of the uncertainty-weighted, least-squares error

$$E(\mathbf{x}) = \sum \left(\frac{y_i^{t} - f_i(\mathbf{x})}{z_i}\right)^2 \tag{1}$$

where $f_i(\mathbf{x})$ is the model prediction of the *i*th target and z_i is a weighting factor for the *i*th target proportional to the uncertainty of the *i*th target, σ_i ; and the posterior uncertainty is approximated via a locally linear surrogate model in the vicinity of the optimized values, \mathbf{x}^* .

$$f(x) \approx f(x^*) + S(x - x^*) \tag{2}$$

where S is a matrix whose elements are given by

$$S_{ij} = \left(\frac{\partial f_i}{\partial x_j}\right)_{\mathbf{x} = \mathbf{x}^*} \tag{3}$$

yielding a covariance matrix,

$$\Sigma = \left(s^T s\right)^{-1} \tag{4}$$

where each row of the normalized sensitivity matrix, s, is equal to each row of S divided by the corresponding weighting factor, z_i . Prediction uncertainties for the QoI(s) can then be evaluated via uncertainty propagation according to

$$\sigma_{QoI} = \left[\mathbf{S}_{QoI} \mathbf{\Sigma} \mathbf{S}_{QoI}^T \right]^{1/2} \tag{5}$$

where S_{QoI} is the sensitivity of the QoI prediction to active parameters. Unlike other inverse UQ methods, the active parameters within MSI can include both molecular parameters (within theoretical kinetics calculations) and physical model parameters (to account for uncertainties in nominal experimental conditions) in addition to rate constant parameters. Furthermore, the data used as targets in MSI can include molecular properties calculated ab initio in addition to rate constant determinations, macroscopic observables (e.g., species mole fractions in an experiment), and any priors for the active model parameters.

After this uncertainty-quantified model based on prior knowledge is created, each predicted observable, $f_i^{(e)}$, in a potential experiment, e, and sensitivity of each observable to model parameters (including the physical model parameters describing the experimental conditions), $S_i^{(e)}$, can be calculated using the model. For the present experiment, the observable is considered to be $\ln(X_{ai}^{(e)})$, where $X_{ai}^{(e)}$ is the JSR outlet

mole fraction for a species to be measured. The relative uncertainty of each potential species mole fraction measurement, $\sigma_i^{(e)}$, notably includes contributions due to a percent reading uncertainty (e.g., 10%), $\sigma_i^{r(e)}$, and a minimum uncertainty (e.g., 10 ppm), $\tilde{\sigma}_i^{m(e)}$, characteristic of each diagnostic via

$$\sigma_i^{(e)} = \sqrt{(\sigma_i^{r(e)})^2 + (\tilde{\sigma}_i^{m(e)}/X_{o,i,p}^{(e)})^2}$$
 (6)

where $X_{o,l,p}^{(e)}$ is the predicted JSR outlet mole fraction for the corresponding species. Physical model parameters for each experiment are also included among the active model parameters with prior uncertainties characteristic of each instrument used to measure them.

Appending the normalized sensitivity matrix, $s^{(e)}$ (defined as before), for each experiment to the previous normalized sensitivity matrix, s, and recalculating the covariance matrix, $\Sigma^{(e)}$, enables evaluation of the QoI prediction uncertainty, $\sigma^{(e)}_{QoI}$, that would result from having run the eth experiment. Once $\sigma^{(e)}_{QoI}$ is calculated for each experiment, the experiment with the lowest estimated $\sigma^{(e)}_{QoI}$ is selected as the best future experiment to perform. To find additional experiments, the procedure is repeated using a normalized sensitivity matrix, s, that includes each of the previously selected experiments. The procedure can be repeated until a certain number of experiments are selected and/or a desired σ_{QoI} is achieved.

2.3. Automated post-processing for experimental data integration into improved models

Once experiments are performed using the computer-controlled experimental apparatus (Section 2.1) at the conditions selected by optimal design (Section 2.2), automated integration of the experimental data into improved models is then achieved via an in-house post-processing script and our MSI software.

This post-processing script retrieves experimental data directly from the instruments, post-processes the measurements and associated metadata, quantifies the associated uncertainties, and produces MSI-compatible YAML files for each experiment. Within the script, the uncertainties for experimental conditions are assigned on the basis of prior detailed analysis of the available equipment (i.e., temperature controller, pressure controller, mass flow controllers, etc.); uncertainties in the measurements are calculated by combining various specified sources of uncertainty from the diagnostic manufacturers and other sources of error such as calibration error or drift (cf. [70]). The YAML files generated contain the values of all measured species, complete metadata describing the experiment (including the reactor temperature, pressure, residence time, and inlet mole fractions), and associated uncertainties for each measurement and physical model parameter.

Thereafter, optimization and inverse UQ within MSI is performed using the new experimental data along with any previous theoretical and experimental data by including the new experimental data among those used in Eqs. (1) and (4).

2.4. Implementation for N_2O kinetics as a demonstration

To demonstrate the effectiveness of this cohesive platform for experimental data selection, generation, and integration, it is implemented here to decipher the main products of the $N_2O + O$ reaction, which has apparently evaded unambiguous determination previously [53]. With the branching ratio uncertainty being dominated by the uncertainty in k_2 , we chose k_2 as the QoI here. While the optimal design procedure can consider previous data, the analysis in the present paper uses no previous theoretical calculations or experimental measurements—to aid in a completely independent investigation of $N_2O + O$ from the analysis of previous data presented in our companion paper [53].

Our analysis here is based on an active kinetic model that adopts the model of Glarborg et al. [51] (with corrected collision efficiencies for key pressure-dependent reactions, e.g., ~2.2 for the He efficiency

Table 1 The list of reactions within the kinetic model, associated prior uncertainties expressed as uncertainty factors (UF), and ratios of rate constants in the MSI (optimized) model to those of the prior model, $k_i^*/k_{i,0}$.

	Reaction	Uncertainty factor	$k_i^*/k_{i,0}$
R1	$N_2O (+M) \Rightarrow N_2 + O (+M)$	3.2	1.19
R2	$N_2O + O \Rightarrow N_2 + O_2$	10	0.05
R3	$N_2O + O \Rightarrow NO + NO$	2.0	1.02
R4	$NO + O (+M) \rightleftharpoons NO_2 (+M)$	2.0	1.36
R5	$NO_2 + O \Rightarrow NO + O_2$	1.2	1.20
R6	$O + O + M \Rightarrow O_2 + M$	1.3	1.00
R7	$N + O_2 \Rightarrow NO + O$	3.2	1.00
R8	$N + NO \Rightarrow N_2 + O$	2.0	1.00
R9	$NO_2 + NO_2 \Rightarrow NO + NO + O_2$	2.0	1.00
R10	$NO_2 + NO_2 \Rightarrow NO + NO_3$	5.0	0.98
R11	$NO_2 + O (+M) \rightleftharpoons NO_3 (+M)$	5.0	0.53
R12	$NO_3 + O \Rightarrow NO_2 + O_2$	10.0	1.00
R13	$NO_2 + NO_3 \Rightarrow NO + NO_2 + O_2$	10.0	1.00
R14	$N_2O + NO \rightleftharpoons N_2 + NO_2$	10.0	1.00

in (R1) [71]), which notably assumes a median value for the k_2/k_3 branching ratio ($k_2/k_3=1$), as the prior model. While the MSI approach allows for a wider variety of active kinetic parameters, only pre-exponential factors are considered here (to enable a purely experimental determination within the limited temperature window of the present experiments). Specifically, the active kinetic parameters for each reaction are $\ln(A_i/A_{i,0})$ (where A_i is the pre-exponential factor for the ith reaction and 0 subscripts refer to the nominal values). Prior uncertainties for each $\ln(A_i/A_{i,0})$ are assumed to follow a normal distribution with two-standard-deviation values equal to $\ln(\text{UF})$. Uncertainty factors, UF = $k_{i,0}/k_{i,lower} = k_{i,upper}/k_{i,0}$, are taken from the compilation of Cornell et al. [65] (if available) or set to 10 (otherwise), cf. Table 1.

In simulating the information content of potential experiments in the optimal design, active physical model parameters are considered with prior uncertainty estimates based on our prior experiments (1% for temperature and pressure, and 5% for mole fraction and residence time). Measurement uncertainties, calculated according to Eq. (6), combine contributions from a 5%-of-reading uncertainty for all measured species and minimum uncertainties specific to each species (50 ppm for N_2O , O_2 , and O_2 and 5 ppm for O_2 and O_3 based on diagnostic specifications and prior experiments [57,65,66]. (Note that, while these estimates are used for experimental design, the post-processing algorithm automatically recalculates and reassigns these uncertainties once experiments have been performed.)

The potential experimental condition space to be explored for optimal design was mapped onto a grid of three temperatures, five residence times, and 25 mole fractions per reactant spanning the ranges given in Table 2 at 1.02 atm pressure. The specific inlet mole fraction ranges for each reactant (e.g., with much lower fractions of NO and NO₂ than N₂O) were chosen to yield outlet mole fractions suitable to each diagnostic. While the apparatus can achieve temperatures over a much wider range (up to ~1200 K), a limited temperature window is considered here based on an initial (ad hoc) screening of conditions along with the desire to reduce all rate constant uncertainties to those of a single temperature-independent factor. In contrast to previous experimental studies used to constrain k_2 , which merely consider uncomplicated mixtures of diluent and N₂O, the condition space explored here also includes "chemical sensitizers" whose inclusion in reactant mixtures might increase the information content of the experiments.

For example, chemical sensitizers could include other O/N species (e.g., N_2 , O_2 , NO, NO_2 , and O_3) without greatly expanding the number of reactions (and associated interpretation uncertainties). Among these, N_2 , O_2 , NO, NO_2 , and their mixtures with inert diluents are commercially available in gas cylinders. Preliminary design calculations revealed minimal gains from N_2 and O_2 in reactant mixtures, such that NO and NO_2 were ultimately selected for optimal design.

Table 2
Range of experimental conditions considered by the optimal design algorithm. Four scenarios were investigated, with increasing complexity of the mixture from scenario \$1.10.54

Scenario	T (K)	P (atm)	τ (s)	X_{N_2O}	X_{NO}	X_{NO_2}
S_1	1000-1100	1.02	0.45-1.5	0.005-0.2	None	None
S_2	1000-1100	1.02	0.45 - 1.5	0.005 - 0.2	0-0.00025	None
S_3	1000-1100	1.02	0.45 - 1.5	0.005 - 0.2	None	0-0.0005
S_4	1000-1100	1.02	0.45 - 1.5	0.005-0.2	0-0.00025	0-0.0005

Table 3 Compiled list of experimental conditions selected by optimal design from scenarios S3 and S4 (ID 1–17, cf. Section 2.4). Note that the equivalent set of diluted conditions (ID 1d–17d, not listed below) was simply obtained by dividing all reactant mole fractions by three. The pressure for all conditions is 1.02 atm.

	*				
ID	T (K)	τ (s)	N ₂ O (%)	NO (ppm)	NO ₂ (ppm)
1	1050	0.45	20.0	0	356
2	1100	1.5	20.0	250	0
3	1050	0.45	20.0	0	0
4	1050	0.45	20.0	10	356
5	1050	0.45	20.0	10	0
6	1100	1.5	6.82	250	180
7	1050	0.45	20.0	11.5	356
8	1050	0.45	20.0	0	10
9	1100	1.5	6.82	250	214
10	1050	0.45	20.0	11.5	0
11	1050	0.45	20.0	0	356
12	1100	1.5	20.0	0	0
13	1050	0.45	20.0	0	0
14	1050	0.45	20.0	0	300
15	1050	0.45	20.0	0	10
16	1050	0.45	20.0	0	11.9
17	1100	1.5	5.85	0	422

The optimal design procedure is implemented for four different condition spaces of varied complexity in mixture composition to ascertain the utility of many-component mixtures and identify especially effective "chemical sensitizers": (S1) $\rm N_2O/He$, (S2) $\rm N_2O/NO/He$, (S3) $\rm N_2O/NO_2/He$, and (S4) $\rm N_2O/NO/NO_2/He$. The procedure was also implemented for five different sets of measured species to ascertain the utility of measuring more species.

Then, experiments were performed for three sets of conditions. First, experiments were performed for a set of conditions (ID 1–17, Table 3) compiled from the first 10 experiments chosen by optimal design from S3 and S4 (the two most effective mixture scenarios), where some conditions from S3 were removed if they were also selected from S4 (resulting in a list of only 17 conditions). Second, experiments were performed for a set of conditions (ID 1d–17d) identical to the first set in every way except that the reactant mole fractions were reduced three-fold—in order to detect any influence from wall reactions, which have influenced some previous intermediate-temperature experiments [51,72]. Third, experiments were performed for a set of conditions identical to the most effective experiment identified (ID1) except that the inlet mole fraction of NO₂, which was found to be the most effective "chemical sensitizer" (cf. Fig. 2), was varied.

Based on the conditions selected, only the IR, ECC, and GC diagnostics were used; the IR detector measured NO_2 , ECC measured NO_2 , and GC measured NO_2 , N_2O_2 , N_2O_3 , and NO_3 . Multi-point GC calibrations were performed over the full range of relevant mole fractions for each species before any experiments were conducted and tested after all experiments were completed—enabling quantification of the calibration drift. The zero and span values for the IR detector and ECC were tested and recalibrated in between all experiments (similar to our previous work)—indicating negligible calibration drift. Calibrations for each diagnostic were tested for linearity and for dependence on the N_2O mole fraction up to 20% (revealing negligible effects). These uncertainties, measured noise, and estimated minimum detectable mole fractions of each diagnostic are reported in Table 4. Physical model parameter

Table 4

Estimated measurement uncertainties specific to each diagnostic instrument. Entries with — indicate uncertainty contribution is negligible compared to other sources of uncertainty. Note that calibrations for species measured on the GC are multipoint calibrations (where a range of mole fractions were used to generate a calibration curve), such that measurement error due to calibration, which is therefore a function of the measurement itself, cannot be easily tabulated below but is included in the estimated uncertainty for each data point (and reflected in Tables S1–S6 in the Supplementary Material). In all cases, the combined uncertainties for each data point are given in the Supplementary Material.

Observable	N_2O^a	$N_2^{\ a}$	NO ^a	NOc	NO_2^b	O_2^a
Calibration	Multi- point	Multi- point	Multi- point	1500 ppm ±2.3%	50.0 ppm ±6.4%	Multi- point
Drift	±1%	±1%	±1%	_	_	±1%
Linearity	±1%	±1%	±1%	±2%	±10%	_
Noise (1σ)	±5%	±2%	$\pm 0.5\%$	±1%	±1%	±2%
Min. Detectable	50 ppm	50 ppm	50 ppm	1 ppm	5 ppm	20 ppm

- ^a Gas chromatography (GC)
- b Infrared absorption (IR)
- c Electrochemical cell (ECC)

uncertainties were also reassessed, indicating reactant mole fraction uncertainties of 2% (instead of 5% used in the optimal design) and uncertainties for temperatures, pressures, and residence times of 1%, 1%, and 5%, respectively, (as used in the optimal design). Independent tests using a DryCal flow meter confirmed the calibration for each MFC to be accurate within 1%. All experimental data and uncertainties are tabulated in the Supplementary Material.

Inverse UQ is then performed based on the first and second experimental datasets to generate an improved kinetic model. In principle, the improved model could be then subjected to another iteration of optimal design, experimentation, and inverse UQ (i.e., an iterative approach similar to Lehn et al. [23]). However, optimal design performed for the model optimized against the dataset described above revealed minimal gains from additional experiments.

3. Results and discussion

3.1. Experiments selected by optimal design

The estimated reduction in k_2 uncertainty from experiments selected by optimal design from each mixture scenario (cf. Table 2) shown in Fig. 2 illustrates several key ideas. First, only a few (optimally selected) experiments are required to achieve substantial estimated uncertainty reductions. Second, the estimated uncertainty reduction is much greater for mixtures containing more distinct reactants (e.g., NO and/or NO₂)—with notable gains over the N₂O/diluent mixtures used in previous experiments. Third, the estimated uncertainty reductions are greater for any mixtures that include NO₂. In fact, mixtures with both NO and NO₂ are only marginally better than mixtures just doped with NO₂—such that experiments including NO₂ as a reactant appear particularly effective in constraining k_2 .

For the purposes of illustrating the utility of measuring multiple species simultaneously, the experimental design procedure was also implemented for scenario S1 (i.e., $N_2 \mbox{O/He}$ mixtures) with varied number of measured species. The estimated uncertainty reductions, shown in Fig. 3, demonstrate the value of measuring many different species in each experiment. Furthermore, while measuring O_2 in addition to $N_2 \mbox{O}$, NO, and N_2 yields negligible estimated gains, measuring NO_2 in addition to the other species yields notably greater uncertainty reductions.

To aid in understanding these trends as well as the specific conditions selected, it is useful to examine the values for a factor defined by

$$\hat{S}_{ij} = S_{ij} \frac{\sigma_j}{\sigma_i} \tag{7}$$

which reflects the sensitivity of the *i*th measurement to the *j*th model parameter times the *j*th model parameter uncertainty divided by the *i*th

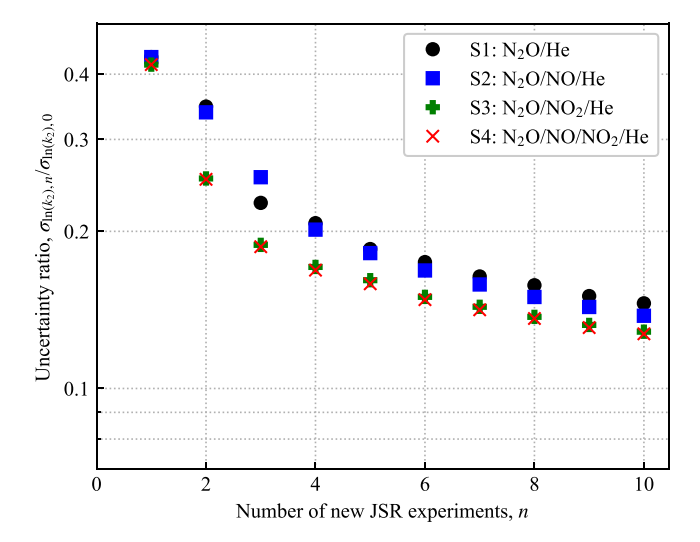


Fig. 2. Ratio of the estimated uncertainty in $\ln(k_2)$ after n experiments to that of the prior model (i.e., n = 0) as a function of the number of new JSR experiments, n, selected by the optimal design algorithm. Results are shown for each of the four scenarios of Table 2 considering N₂O, NO, N₂, O₂, and NO₂ to be measured in each experiment.

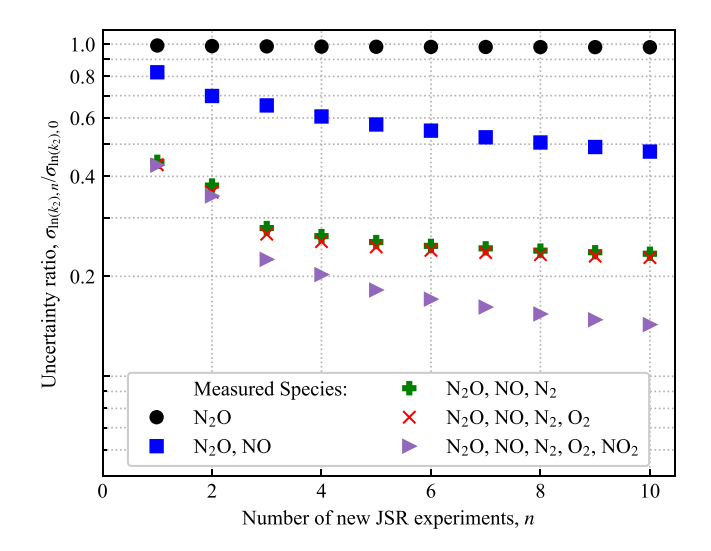


Fig. 3. Ratio of the estimated uncertainty in $\ln(k_2)$ after n experiments to that of the prior model (i.e., n=0) as a function of the number of new JSR experiments, n, selected by the optimal design algorithm. Results are shown for scenario S1 from Table 2 under five different sets of species considered to be measured.

measurement uncertainty. The values of this parameter, shown in Fig. 4 for each species to be measured in the first five selected experiments and the five most important reactions (R1–R5), reflect the expected information content of a specific measurement.

For context, a $|\hat{S}_{ij}|$ much less than 1 implies minimal information about the jth parameter can be gained from the ith measurement; and higher $|\hat{S}_{ij}|$ values imply that more information is provided by the ith measurement about the jth parameter (albeit in a manner coupled to other parameters with high $|\hat{S}_{ij}|$). For example, measurements of N₂O, which is predicted to maintain outlet mole fractions similar to the inlet mole fractions, have low $|\hat{S}_{ij}|$ and would therefore provide minimal information; by contrast, $|\hat{S}_{ij}|$ for measurements of other species can reach ~ 10 and would therefore be very informative of specific combinations of parameters.

Qualitatively, the experiments selected for mixtures of N₂O/He and N₂O/NO/He show very similar behavior, with the sign of \hat{S}_{ij} being generally the same for each reaction for a given measured species. By

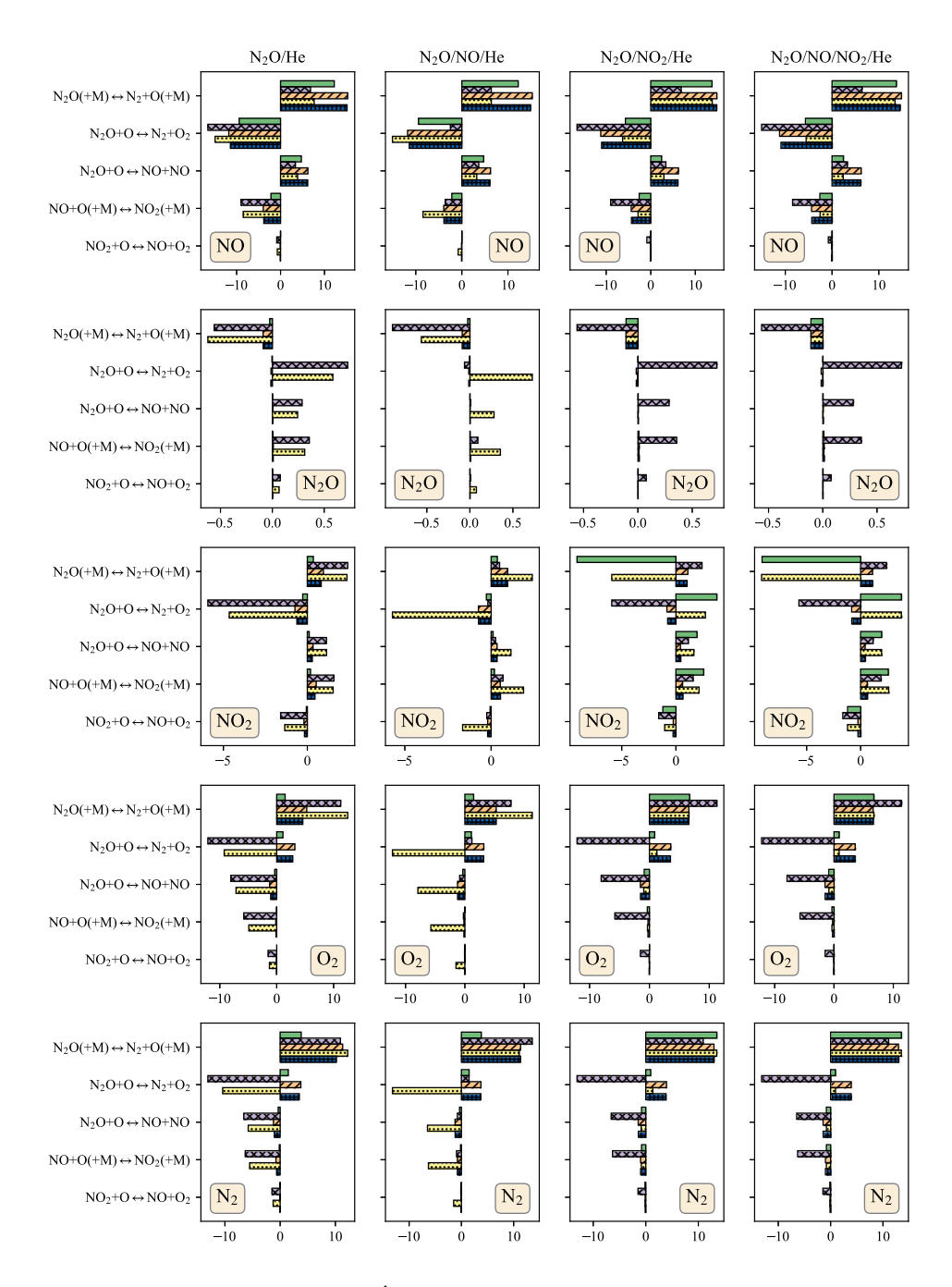


Fig. 4. Values (on the x-axis) for doubly-uncertainty-weighted sensitivities, $\hat{S}_{ij} = S_{ij}\sigma_j/\sigma_i$, of the five species to be measured (in different rows of panels) to the five most important reactions (labeled on the y-axis of each panel) for the first five selected experiments (in different bars for each reaction in each panel) in each of the four scenarios of Table 2 (in different columns of panels).

contrast, mixtures doped with NO_2 display different behavior specifically for measurements of NO_2 . In addition to having higher absolute values of \hat{S}_{ij} , the sign of the sensitivity of NO_2 measurements to k_1 and k_2 in S3 and S4 varies from experiment to experiment. Notably, in contrast to all other species and in contrast to all species for S1 and S2 (without NO_2 addition), the sensitivity of predicted NO_2 outlet mole fraction to k_1 is negative for experiments with NO_2 (the first and fourth selected experiments in S3 and S4). Therefore, measuring NO_2 in reactant mixtures with NO_2 aids in removing the correlation among rate constants in the information provided by measurements of other species and in other mixtures (explored further in Section 3.3). Altogether,

Figs. 2-4 suggest a unique value in measuring NO_2 in mixtures with NO_2 addition—which has not been done in any previous experiments.

3.2. Experimental results and model comparisons

Given that scenarios with NO_2 addition (S3 and S4) were found most effective, experiments were performed for the optimally selected conditions from S3 and S4 (ID 1–17, Table 3) and for the equivalent "diluted" conditions (ID 1d–17d, cf. Section 2.4). Inverse UQ based on these data and the priors for the rate constant parameters (cf. Table 1) and physical model parameters (cf. Section 2.4) yields an (optimized) MSI model (with rate constant adjustments indicated in Table 1) that

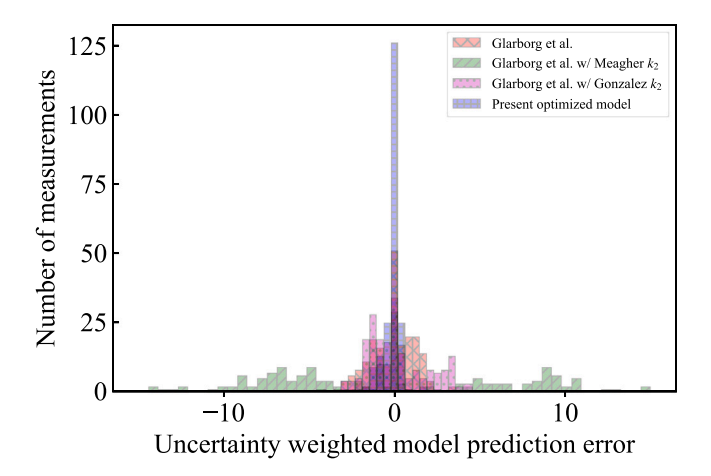


Fig. 5. Distribution of uncertainty-weighted errors, $(y_i^t - f_i)/\sigma_i$, for model predictions, f_i , relative to the present experimental measurements, y^t , using several models: the prior model (adopted from Glarborg et al. [51]) (red), the prior model with k_2 from Meagher and Anderson [52] (green), the prior model with k_2 from González et al. [73] (pink), and the MSI model (blue). (For interpretation of the references to color in this figure legend, the reader is referred to the web version of this article.)

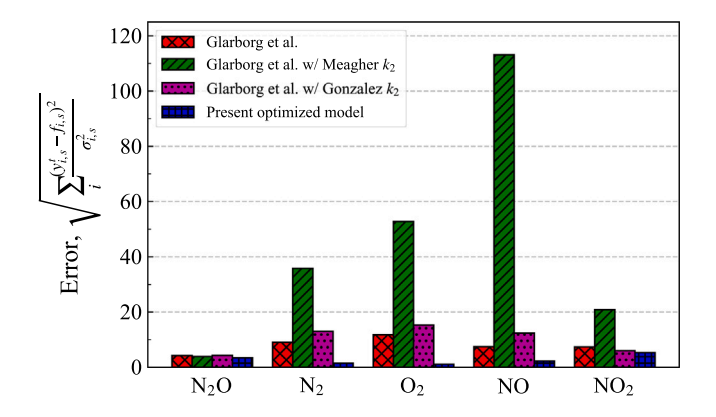


Fig. 6. Square root of the sum of squared uncertainty-weighted errors for model predictions, $f_{l,s}$, relative to the present experimental measurements, y^t , for each species s using several models: the prior model (adopted from Glarborg et al. [51]) (red), the prior model with k_2 from Meagher and Anderson [52] (green), the prior model with k_2 from González et al. [73] (pink), and the MSI model (blue). (For interpretation of the references to color in this figure legend, the reader is referred to the web version of this article.)

is generally consistent with the present data and priors. Specifically, all rate and physical model parameters lie within their prior uncertainties except for k_2 , where the 5-order-of-magnitude spread in previously proposed values at intermediate temperatures suggests a much larger prior uncertainty anyway. Notably, k_2 in the MSI model is substantially reduced from that of the prior model (adopted from Glarborg et al. [51]), yielding a branching ratio for the N_2O+O that greatly favors NO+NO as the main products (consistent with González et al. [51]).

The agreement of this MSI model with the present experimental data is excellent, with uncertainty-weighted errors, $(y_i^t - f_i)/\sigma_i$, generally less than 1 and tightly centered about ~0 with a standard deviation of ~0.5 (consistent with experimental uncertainty estimates reflecting the 2σ level). Furthermore, with the exception of NO₂, whose values are close to the minimum detection error in many diluted experiments, the MSI model reproduces the experiments at undiluted (ID 1–17) and diluted (ID 1d–17d) conditions with very similar uncertainty-weighted error statistics for each species—suggestive of minimal impact of wall reactions.

Statistics for the uncertainty-weighted errors against the experimental data for the MSI model are shown in Figs. 5-7, where three other

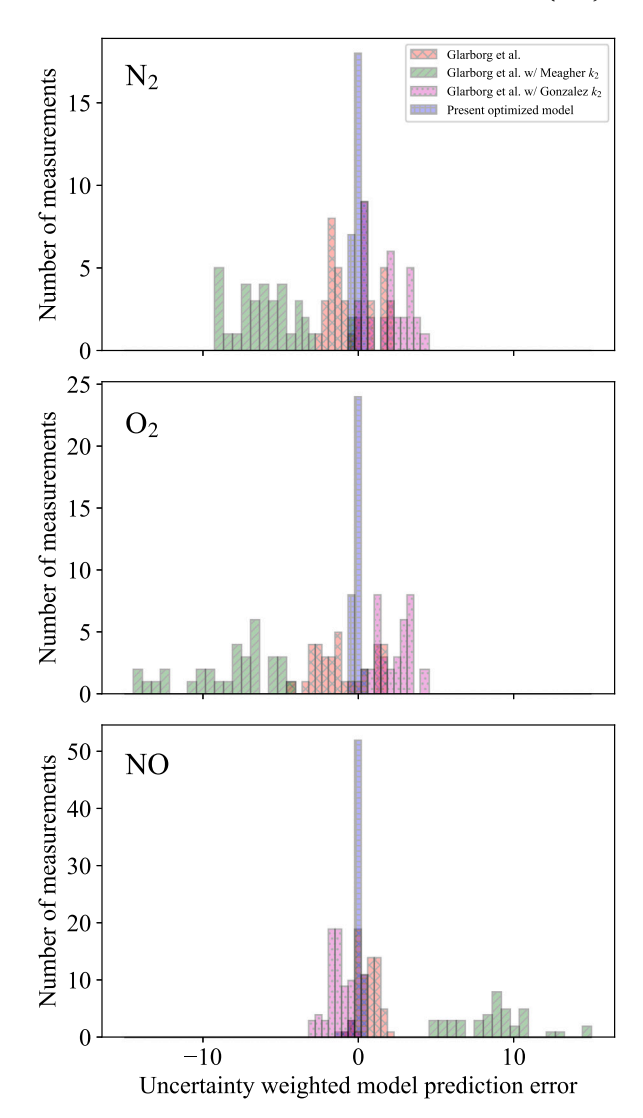


Fig. 7. Distribution of uncertainty-weighted errors, $(y_i^t - f_i)/\sigma_i$, for model predictions, f_i , relative to the present experimental measurements, y^t , for N_2 , O_2 , and NO using several models: the prior model (adopted from Glarborg et al. [51]) (red), the prior model with k_2 from Meagher and Anderson [52] (green), the prior model with k_2 from González et al. [73] (pink), and the MSI model (blue). (For interpretation of the references to color in this figure legend, the reader is referred to the web version of this article.)

models are also shown for comparison: (1) the prior model (adopted from Glarborg et al. [51]), (2) the prior model with k_2 from Meagher and Anderson [52], and (3) the prior model with k_2 from González et al. [73]. Compared to the MSI model, the uncertainty-weighted errors for the other three models are noticeably larger. By contrast to the MSI model, prior model, and prior model with k_2 from González et al. [73] (which all have $k_2/k_3 \le 1$), the uncertainty-weighted errors are especially large for the model with k_2 from Meagher and Anderson [52] and, even more so, for a model with k_2 from Pham and Lin [74] (not shown), which both have $k_2/k_3 >> 1$.

Inspection of the sums of the squared uncertainty-weighted errors for each species (shown in Fig. 6) reveals that the majority of these errors for the models with k_2 from Meagher and Anderson [52] (or Pham and Lin [74]) is concentrated in measurements of N_2 , O_2 , and NO—which would be consistent with errors in the k_2/k_3 branching ratio in these models. In fact, the distributions of uncertainty-weighted errors for N_2 , O_2 , and NO (shown in Fig. 7) further support this notion. Specifically, the prediction errors $(y_i^t - f_i)/\sigma_i$ for the models with k_2 from Meagher and Anderson [52] (or Pham and Lin [74]) are always

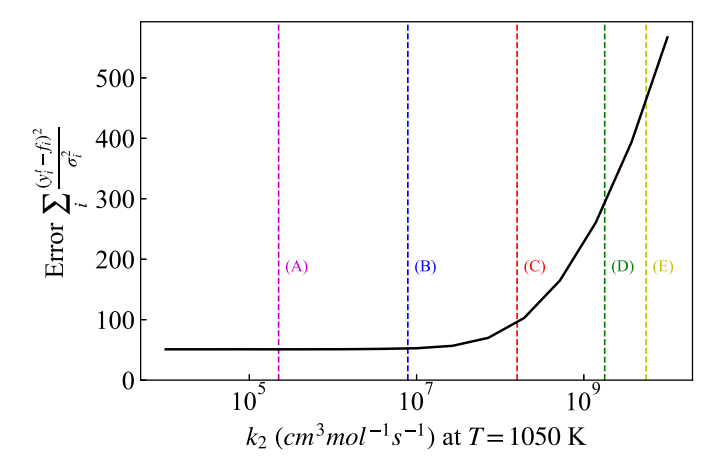


Fig. 8. Square root of the sum of squared uncertainty-weighted errors for model predictions, f_i , relative to the present experimental measurements, y^i , for MSI models optimized for a range of fixed values of k_2 at 1050 K. Vertical dashed lines indicate k_2 (1050 K) from (A) González et al. [73], (B) the MSI model optimized with k_2 among the active parameters, (C) Glarborg et al. [51], (D) Meagher and Anderson [52], and (E) Pham and Lin [74].

negative for N_2 and O_2 but positive for NO. That is, the models with k_2 from Meagher and Anderson [52] or Pham and Lin [74] overpredict N_2 and N_2 (the products of (R2)) and underpredict NO (the products of (R3)), which is consistent with k_2/k_3 being too high in those models.

That being said, while the discussion above seems to imply that the data support lower values of k_2/k_3 , previous experimental data could of course be equally well reproduced with k_2/k_3 values much greater than 1 *and* much less than 1—depending on the rate constants for other reactions in the model [53]; and, except for the MSI model, all models in Figs. 5–7 differ only in their values for k_2 .

Therefore, to ensure that the present conclusions are not model-dependent in the same way as previous experimental studies, a series of alternative optimizations were carried out where k_2 was fixed at a series of different values while all other model parameters were optimized. The sums of squared uncertainty-weighted errors for this series of optimizations, shown in Fig. 8, reveal that the minimum residual errors can be achieved for a broad range of k_2 —at least for k_2 (1050 K) lower than $\sim 10^7$ cm³ mol $^{-1}$ s $^{-1}$, which notably encompasses the theoretical calculations of González et al. [73]. For k_2 below this value, the present experiments alone cannot distinguish among different k_2 values (which also poses a challenge for typical methods for quantifying posterior uncertainties, including that used here). (That being said, consideration of theoretical calculations [73] among the data, as done in our companion paper [53], leads to a well-defined optimum value with a more easily quantifiable posterior uncertainty.)

However, for k_2 values higher than $\sim 10^7 \, \mathrm{cm^3 \ mol^{-1} \ s^{-1}}$, the residual errors rapidly increase with increasing k_2 —rising from a factor of two higher for $k_2 \approx 10^8 \, \mathrm{cm^3 \ mol^{-1} \ s^{-1}}$ (corresponding to $k_2/k_3 \approx 1$ as in the prior model adopted from Glarborg et al. [51]) to a factor of ~ 10 higher for k_2 values from Meagher and Anderson [52] and Pham and Lin [74]. In other words, branching ratios k_2/k_3 greater than 1 are simply inconsistent with the experimental data regardless of the choices of rate constants for the other reactions.

Consequently, the present experiments seem to have constrained k_2 at intermediate temperatures in a manner that previous experiments have not. Notably, the present experiments are apparently the first to employ varied NO_2 addition, which the optimal design results of Section 3.1 reveal to have unique advantages in constraining k_2- motivating the following section intended to understand the role of NO_2 addition in deciphering the main products of $\mathrm{N}_2\mathrm{O}+\mathrm{O}.$

3.3. Further analysis of NO2 addition

Examination of the inlet NO_2 mole fraction dependence aids in both visually assessing the performance of the models with different k_2 and further understanding why NO_2 addition is as effective as the optimal design results indicate. Consistent with the statistics reported in Section 3.2, Fig. 9 reveals that models with lower k_2 better reproduce the experimentally observed values and trends with inlet NO_2 . Even among the models with lower k_2 values (including the prior model, MSI model, and model with k_2 from González et al. [73]), models with $k_2(1050\mathrm{K}) \ll \sim 10^8$ cm³ mol $^{-1}$ s $^{-1}$ (the MSI model and model with k_2 from González et al. [73]) better reproduce subtle qualitative features in the measurements such as the lack of inlet NO_2 mole fraction dependence of outlet N_2 mole fractions.

Furthermore, model predictions with high k_2 (from Meagher and Anderson [52] and Pham and Lin [74]) are inconsistent with not only the experimentally observed species mole fractions but also their trends with inlet NO_2 mole fraction. For example, models with high k_2 predict decreasing N_2 with increasing inlet NO_2 (instead of constant N_2 as observed) and constant O_2 with increasing inlet NO_2 (instead of increasing O_2 as observed). The qualitative differences are most pronounced for outlet mole fractions of NO_2 , which exhibited very different sensitivity coefficients with and without inlet NO_2 (Fig. 4). Namely, models with high k_2 underpredict outlet NO_2 by a factor of ~ 10 with 0 inlet NO_2 and overpredict outlet NO_2 by a similar amount with 356 ppm inlet NO_2 .

Analysis of the reactions responsible for production/consumption of each species calculated with the MSI model and the model with k_2 from Meagher and Anderson [52] (Fig. 10) sheds light on these observations. While both models predict NO_x to be formed exclusively via (R3) (and exchanged between NO and NO_2 via R4 and R5), the two models show important differences in the reactions responsible for the other main species (N_2O , N_2 , O_2 , and O). Notably, in the MSI model predictions, (R2) is not a significant production or consumption pathway for any species— N_2O is consumed mostly by (R1) and partially by (R3), N_2 is exclusively formed via (R1), O_2 is exclusively formed via R4, and O is consumed mostly by R4 and R5 and partially by (R3). The fact that N_2 is exclusively formed via (R1) serves to explain the lack of inlet NO_2 dependence in the MSI model—with the outlet N_2O mole fraction remaining close to its inlet value, the rate of (R1) and likewise the rate of N_2 production is independent of inlet NO_2 .

As an aside, the fact that (R2) is not a significant production or consumption pathway for any species also serves to explain the fact that the experiments cannot distinguish among k_2 values that are sufficiently low (cf. Fig. 8). After all, the rates of production of all measured species that are reactants (N₂O) or products (N₂ and O₂) of (R2) have two distinct terms

$$\hat{\omega}_{N_2O} = -k_1[N_2O] - (k_2 + k_3)[N_2O][O]$$
 (8)

$$\hat{\omega}_{N_2} = k_1[N_2O] + k_2[N_2O][O]$$
(9)

$$\hat{\omega}_{O_2} = k_2[N_2O][O] + k_5[NO_2][O]$$
 (10)

Given the typical mole fractions observed for NO (\sim 700 ppm) and NO₂ (\sim 20 ppm), the reasonably established values for k_1 , k_4 , and k_5 (of $1.4 \times 10^{-2} \text{ s}^{-1}$, $7 \times 10^{10} \text{ cm}^3 \text{ mol}^{-1} \text{ s}^{-1}$, and $3.0 \times 10^{12} \text{ cm}^3 \text{ mol}^{-1} \text{ s}^{-1}$ for 1050 K, 1 atm, and He bath), and the fact that O is essentially a quasi-steady-state species,

$$[O] \approx \frac{k_1[N_2O]}{k_2[N_2O] + k_3[N_2O] + k_4[NO] + k_5[NO_2]}$$
(11)

the k_2 term in each of these equations is only significant when $k_2 > \sim 10^8$ cm³ mol⁻¹ s⁻¹ (consistent with the results of Fig. 8). This serves to explain the only minor qualitative differences for inlet NO₂ dependence of N₂ for the prior model (where $k_2 \approx 10^8$ cm³ mol⁻¹ s⁻¹), which

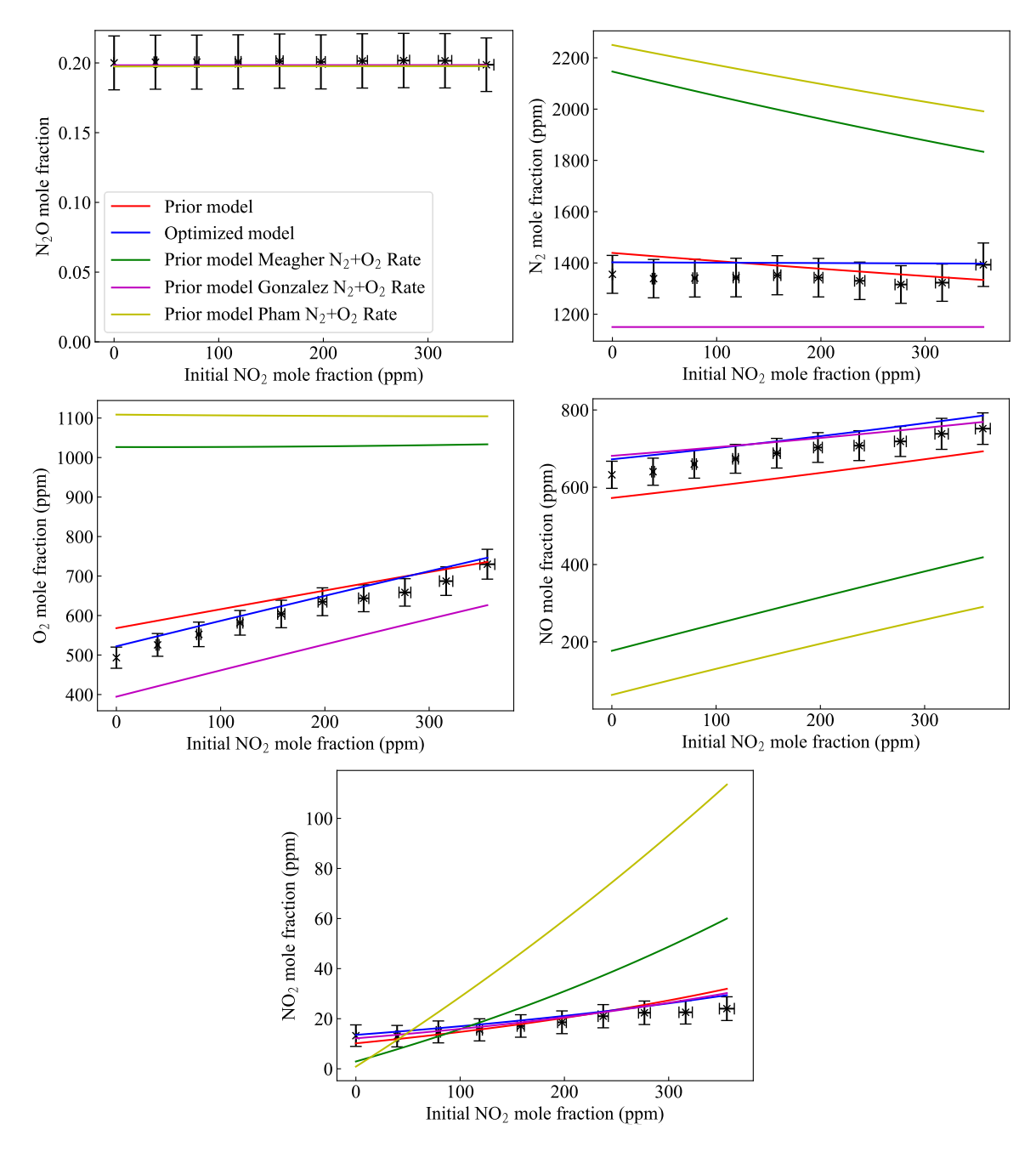


Fig. 9. Species mole fractions in the outlet mixture as a function of NO_2 mole fraction in the inlet (reactant) mixture (along with 20% N_2O and balance He). Symbols indicate the present experimental measurements and lines indicate model predictions using the prior model (adopted from Glarborg et al. [51]) (red), the MSI model (blue), the prior model with k_2 from Meagher and Anderson [52] (green), the prior model with k_2 from González et al. [73] (pink), and the prior model with k_2 from Pham and Lin [74] (yellow). (For interpretation of the references to color in this figure legend, the reader is referred to the web version of this article.)

predicts a decreasing dependence, and the MSI model and model with k_2 from González et al. [73] (where $k_2 <\sim 10^7 \text{ cm}^3 \text{ mol}^{-1} \text{ s}^{-1}$), which predict no dependence (consistent with the data).

On the other hand, in simulations using the model with k_2 from Meagher and Anderson [52], (R2) yields comparable contributions to (R1) in N₂O consumption and N₂ production and dominates O₂ production and O consumption. With the correspondingly higher rates of consumption predicted for O, the predicted O mole fractions are much lower and, therefore, the rates of NO formation (and NO₂ consumption) are also much lower. Furthermore, with significant contributions of (R2) to N₂ and O₂, the reduced O mole fractions for high inlet NO₂, which consumes O via R5 to form O₂ and NO, lead to reduced rates of (R2) and consequently lower N₂ with increasing inlet NO₂ but constant O₂ with increasing inlet NO₂ given that (R2) and R5 both produce O₂.

The impact of the mechanistic differences for $k_2 \gg \sim 10^8$ cm³ mol $^{-1}$ s $^{-1}$ on the inlet NO $_2$ dependence of outlet NO $_2$ mole fractions is particularly interesting (especially in light of the sensitivity coefficients for outlet NO $_2$ in scenarios with NO $_2$ addition). For conditions where NO $_2$ is produced on the net inside the reactor (e.g., for 0 inlet NO $_2$), models with high k_2 values, which yield lower NO and O mole fractions (and likewise lower NO $_2$ production via R4), significantly underpredict the outlet NO $_2$ mole fraction. On the other hand, for conditions where NO $_2$ is consumed on the net inside the reactor (e.g., for 356 ppm inlet NO $_2$), models with high k_2 values, which yield lower O mole fractions (and likewise lower NO $_2$ consumption via R5), significantly overpredict the outlet NO $_2$ mole fraction.

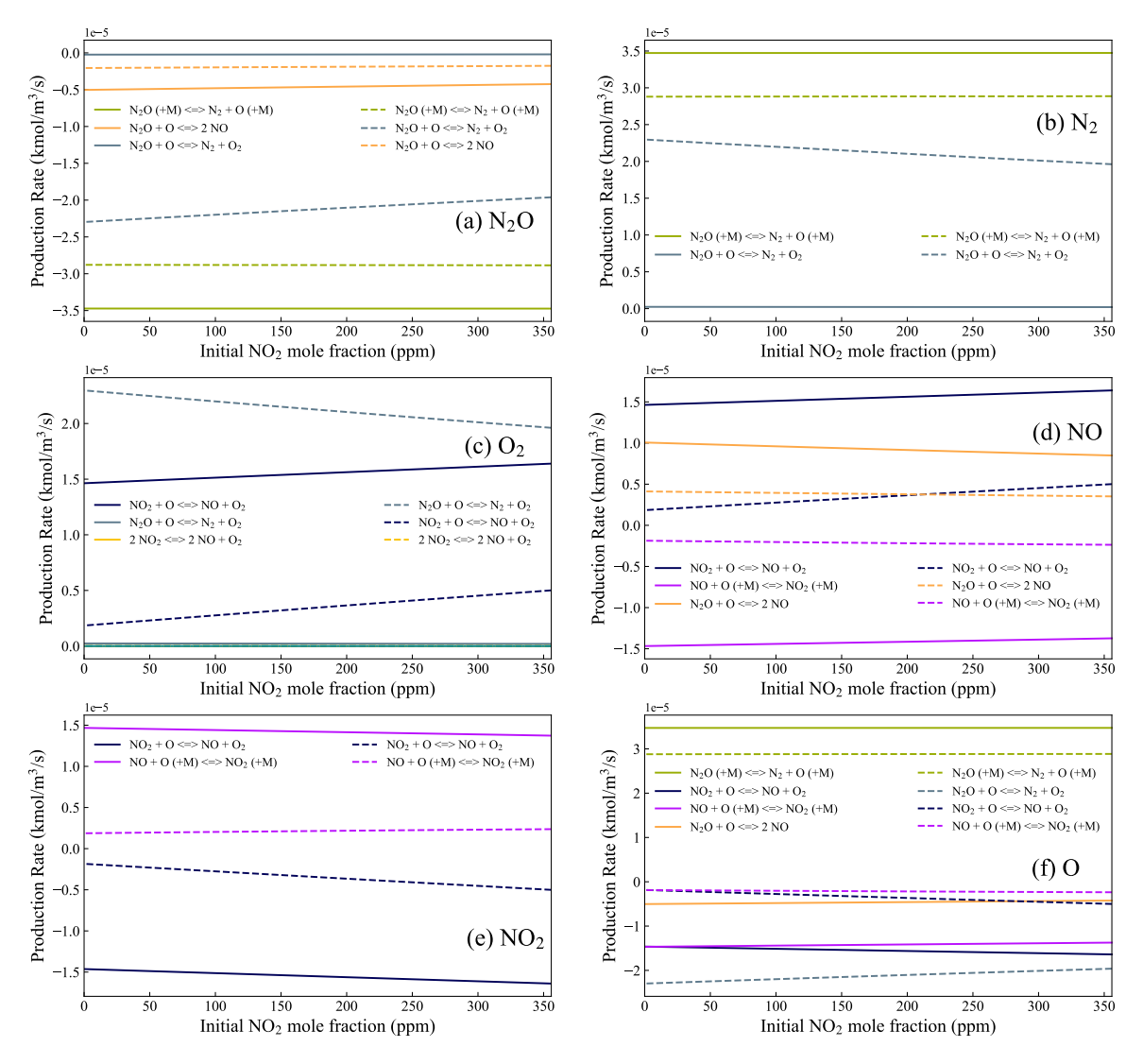


Fig. 10. Rates of production for key species for the conditions of Fig. 9. Solid lines are calculated using the MSI model, while dashed lines are calculated using the prior model with k_2 from Meagher and Anderson [52].

Altogether, these results serve to explain why NO2 addition (which has not been employed in previous studies of k_2) appears to be especially useful to deciphering the main products of N₂O + O in the present experiments in a way that previous experiments without NO₂ addition have not. In particular, the present experiments appear to preclude the possibility that N₂ + O₂ are the dominant products at intermediate temperatures as reported by Pham et al. [55,74] and Meagher and Anderson [52]. Instead, the present experiments can only be explained with k_2 values that are at most $\sim 10^8$ cm³ mol⁻¹ s⁻¹ (corresponding to $k_2/k_3 \approx 1$, as suggested by Glarborg et al. [51]) as an upper limit, though the experimental values and trends with NO2 are more closely reproduced using k_2 that are much lower ($\sim 10^7$ cm³ mol⁻¹ s-1 or below)—such as those from the theoretical study of González et al. [73]; MSI analysis of the present data here; and MSI analysis of the present data, theoretical data of González et al. [73], and raw data from previous experimental studies in our companion study [53].

4. Concluding remarks

A platform for rapid kinetic model refinement and validation involving selection, generation, and integration of experimental data is presented. The platform combines optimal experimental design, a computer-controlled JSR experimental apparatus, a post-processing code that retrieves data from the instruments and produces self-

contained files with all data and metadata (including uncertainties), and our MSI package for model optimization and uncertainty quantification.

This platform was demonstrated for the rate constant of $N_2O + O \Rightarrow N_2 + O_2$ (R2) as the QoI to determine the main products of the $N_2O + O$ reaction at intermediate temperatures. The results from optimal design reveal that reactant mixtures with more species and measurements for more species yield greater reductions in the QoI uncertainty. The optimal design results, in particular, identified that measurements of outlet NO_2 mole fractions for varied inlet NO_2 mole fraction would be especially effective. Experiments were then conducted for three sets of conditions: (1) a set of conditions identified by optimal design, (2) an analogous set with higher dilution (to ascertain any wall reaction influences, of which we found none), and (3) a set with varied inlet NO_2 mole fraction (to visualize and explain the unique advantages of NO_2 addition to the reactant mixture).

All told, model predictions using higher proposed values of k_2 (e.g., from Meagher and Anderson [52] and Pham and Lin [74]) are simply inconsistent with the experimental data both quantitatively and qualitatively—regardless of the choices of rate constants for the other reactions. Instead, the data support $k_2(1050~{\rm K}){<}{\sim}10^8~{\rm cm}^3~{\rm mol}^{-1}~{\rm s}^{-1}$ (consistent with González et al. [73]), which effectively preclude N₂ + O₂ as the main products.

Further analysis revealed the reasons (from a chemical perspective) for the effectiveness of mixtures containing NO_2 as a "chemical sensitizer"—a term we use to refer to a species not present as a reactant in the QoI that serves to increase information about the QoI. For example, (R1) accelerates formation/consumption of NO_2 and (R2) slows formation/consumption of NO_2 without/with NO_2 addition—leading to opposite sensitivities of outlet NO_2 to each reaction with and without NO_2 addition (and, therefore, serving to remove common correlations in the data). Consequently, models with higher k_2 underpredict outlet NO_2 for low inlet NO_2 , for which NO_2 is produced on the net, and overpredict outlet NO_2 for high inlet NO_2 , for which NO_2 is consumed on the net.

Altogether, the present experimental platform achieved a goal that no previous experiment over the past several decades appears to have done: decipher the main products of N_2O+O at intermediate temperatures. The analysis indicated that this success can be largely attributed to the present inclusion of NO_2 as a reactant and analyte—neither of which were included in previous experimental studies and both of which are consistent with the unique design principles of our experimental platform (many-component reactants and many-species diagnostics)—altogether implying that this experimental platform is likely to be a key tool in accelerating scientific discovery and kinetic model development.

More broadly, merging the present experimental platform—combining optimal design, computer-controlled experiments, automated data post-processing, and inverse UQ—with existing computational platforms implementing automated mechanism generation and automated theoretical kinetics calculations, in principle, would create a rapid, semi-autonomous platform for model construction, refinement, and validation that incorporates all key elements of the model development process. We envision that such a platform would be invaluable to characterizing the ever-expanding landscape of potential 21st century fuels on the timescales needed to address climate change and other pressing societal issues.

CRediT authorship contribution statement

Mark C. Barbet: Writing – review & editing, Writing – original draft, Software, Methodology, Investigation, Formal analysis, Data curation. Joe Lee: Formal analysis, Data curation. Carly E. LaGrotta: Software. Rodger E. Cornell: Data curation. Michael P. Burke: Writing – review & editing, Writing – original draft, Supervision, Resources, Project administration, Funding acquisition, Conceptualization.

Declaration of competing interest

The authors declare that they have no known competing financial interests or personal relationships that could have appeared to influence the work reported in this paper.

Acknowledgments

The authors gratefully acknowledge support of this research by the National Science Foundation Computational and Data-Enabled Science and Engineering program (CBET-1761491) and Combustion and Fire Systems program (CBET-1944004).

Appendix A. Supplementary data

Supplementary material related to this article can be found online at https://doi.org/10.1016/j.combustflame.2024.113562.

References

- Global primary energy consumption by source—ourworldindata.org, 2023, https: //ourworldindata.org/grapher/global-energy-substitution?stackMode=relative. (Accessed 19-Jun-2023).
- [2] Net Zero by 2050, Int. Energy Agency (2021).
- [3] Assessment of fuel economy technologies for light-duty vehicles, Natl. Res. Counc. (2011).
- [4] Pathways to sustainable energy: Accelerating energy transition in the UNECE region, in: United Nations Economic Commission for Europe, in: Ece Energy Series No. 67, 2020.
- [5] OECD contribution to the united nations commision on sustainable development, Organ. Econ. Co-oper. Dev. 15 (2007).
- [6] S. Som, W. Liu, D.D.Y. Zhou, G.M. Magnotti, R. Sivaramakrishnan, D.E. Longman, R.T. Skodje, M.J. Davis, Quantum tunneling affects engine performance, J. Phys. Chem. Lett. 4 (2013) 2021–2025.
- [7] W. Hwang, J. Dec, M. Sjöberg, Spectroscopic and chemical-kinetic analysis of the phases of HCCI autoignition and combustion for single- and two-stage ignition fuels, Combust. Flame 154 (2008) 387–409.
- [8] R.D. Reitz, Directions in internal combustion research, Combust. Flame 160 (2013) 1–8.
- [9] S. Gkantonas, S. Jella, S. Iavarone, P. Versailles, E. Mastorakos, G. Bourque, Estimation of autoignition propensity in aeroderivative gas turbine premixers using incompletely stirred reactor network modeling, J. Eng. Gas Turbines Power 144 (2022) 101009.
- [10] S. Yousefian, S. Jella, P. Versailles, G. Bourque, R.F.D. Monaghan, A stochastic and Bayesian inference toolchain for uncertainty and risk quantification of rare autoignition events in dry low-emission premixers, J. Eng. Gas Turbines Power 144 (11) (2022) 111015.
- [11] D.J. Vermeer, J.W. Meyer, A.K. Oppenheim, Auto-ignition of hydrocarbons behind reflected shock waves. Combust. Flame 18 (1972) 327–336.
- [12] C.M. Coats, A. Williams, Investigation of the ignition and combustion of n-heptane-oxygen mixtures, Symp. (Int.) Combust. 17 (1979) 611–621.
- [13] P. Dagaut, M. Reuillon, M. Cathonnet, High pressure oxidation of liquid fuels from low to high temperature. 1. n-heptane and iso-octane, Combust. Sci. Technol. 95 (1993) 233–260.
- [14] K. Zhang, C. Banyon, J. Bugler, H.J. Curran, A. Rodriguez, O. Herbinet, F. Battin-Leclerc, C. B'Chir, K.A. Heufer, An updated experimental and kinetic modeling study of n-heptane oxidation, Combust. Flame 172 (2016) 116–135.
- [15] V. Warth, F. Battin-Leclerc, R. Fournet, P.A. Glaude, G.M. Côme, G. Scacchi, Computer based generation of reaction mechanisms for gas-phase oxidation, Comput. Chem. 24 (2000) 541–560.
- [16] M. Liu, A.G. Dana, M.S. Johnson, M.J. Goldman, A. Jocher, A.M. Payne, C.A. Grambow, K. Han, N.W. Yee, E.J. Mazeau, K. Blondal, R.H. West, C.F. Goldsmith, W.H. Green, Reaction mechanism generator v3.0: Advances in automatic mechanism generation, J. Chem. Inf. Model. 61 (2021) 2686–2696.
- [17] L.J. Broadbelt, S.M. Stark, M.T. Klein, Computer generated pyrolysis modeling: On-the-fly generation of species, reactions, and rates, Indust. and Eng. Chem. Res. 33 (1994) 790–799.
- [18] L. Cai, S. Jacobs, R. Langer, F. vom Lehn, K.A. Heufer, H. Pitsch, Auto-ignition of oxymethylene ethers (OME_n, n=2-4) as promising synthetic e-fuels from renewable electricity: shock tube experiments and automatic mechanism generation, Fuel 264 (2020) 116711.
- [19] X. Huan, Y.M. Marzouk, Simulation-based optimal Bayesian experimental design for non-linear systems, J. Comput. Phys. 232 (2013) 288–317.
- [20] D.A. Sheen, J.A. Manion, Kinetics of the reactions of H and CH₃ radicals with n-butane: An experimental design study using reaction network analysis, J. Phys. Chem. A 118 (2014) 4929–4941.
- [21] É. Válko, M. Papp, M. Kovács, T. Varga, I. Gy. Zsély, T. Nagy, T. Turányi, Design of combustion experiments using differential entropy, Combust. Theory Model. 26 (2022) 67–90.
- [22] B. Yang, Towards predictive combustion kinetic models: Progress in model analysis and informative experiments, Proc. Combust. Inst. 38 (2021) 199–222.
- [23] F. vom Lehn, L. Cai, H. Pitsch, Iterative model-based experimental design for efficient uncertainty minimization of chemical mechanisms, Proc. Combust. Inst. 38 (2021) 1033–1042.
- [24] P.L. Bhoorasingh, B.L. Slakman, F.S. Khanshan, J.Y. Cain, R.H. West, Automated transition state theory calculations for high-throughput kinetics, J. Phys. Chem. A 121 (2017) 6896–6904.
- [25] M. Keçeli, S.N. Elliott, Y.P. Li, M.S. Johnson, C. Cavallotti, Y. Georgievskii, W.H. Green, M. Pelucchi, J.M. Wozniak, A.W. Jasper, S.J. Klippenstein, Automated computational thermochemistry for butane oxidation: A prelude to predictive automated combustion kinetics, Proc. Combust. Inst. 37 (2019) 363–371.
- [26] R. Van de Vijver, J. Zádor, KinBot: Automated stationary point search on potential energy surfaces, Comp. Phys. Comm. 248 (2019) 106947.
- [27] J. Zádor, C. Martí, R. Van de Vijver, S.L. Johansen, Y. Yang, H.A. Michelson, H.N. Najm, Automated reaction kinetics of gas-phase organic species over multiwell potential energy surfaces, J. Phys. Chem. A. 127 (2023) 565–588.
- [28] M. Frenklach, Transforming data into knowledge-process informatics for combustion chemistry, Proc. Combust. Inst. 31 (2007) 125–140.

- [29] K. Braman, T.A. Oliver, V. Raman, Bayesian analysis of syngas chemistry models, Combust. Theory Mod. 17 (2013) 858–887.
- [30] T. Turányi, T. Nagy, I.G. Zsély, M. Cserháti, T. Varga, B.T. Szabó, I. Sedyó, P.T. Kiss, A. Zempléni, H.J. Curran, Determination of rate parameters based on both direct and indirect measurements. Int. J. Chem. Kin. 44 (2012) 284–302.
- [31] H. Wang, D.A. Sheen, Combustion kinetic model uncertainty quantification, propagation and minimization, Prog. Energy Combust. Sci. 47 (2015) 1–31.
- [32] M.P. Burke, Harnessing the combined power of theoretical and experimental data through multiscale informatics, Int. J. Chem. Kinet. 48 (2016) 212–235.
- [33] P.T. Lynch, T.P. Troy, M. Ahmed, R.S. Tranter, Probing combustion chemistry in a miniature shock tube with synchrotron VUV photo ionization mass spectrometry, Anal. Chem. 87 (2015) 2345–2352.
- [34] M.E. Fuller, M. Skowron, R.S. Tranter, C.F. Goldsmith, A modular, multidiagnostic, automated shock tube for gas-phase chemistry, Rev. Sci. Instrum. 90 (2019) 064104.
- [35] M.S. Johnson, A.G. Dana, W.H. Green, A workflow for automatic generation and efficient refinement of individual pressure-dependent networks, Combust. Flame 257 (2023) 112516.
- [36] S. Harris, C.E. LaGrotta, M.C. Barbet, M.P. Burke, R.H. West, Accelerating the process of combustion mechanism discovery through correlated uncertainty and sensitivity analysis, AIChE Annu. Meet. (2022).
- [37] M.P. Burke, F.L. Dryer, Y. Ju, Assessment of kinetic modeling for lean H₂/CH₄/O₂/diluent flames at high pressures, Proc. Combust. Inst. 33 (2011) 905–912
- [38] J.J. Scire Jr., R.A. Yetter, F.L. Dryer, Flow reactor studies of methyl radical oxidation reactions in methane-perturbed moist carbon monoxide oxidation at high pressure with model sensitivity analysis, Int. J. Chem. Kinet. 33 (2001) 75–100.
- [39] P.G. Ashmore, B.J. Tyler, Reaction of hydrogen atoms with nitrogen dioxide, Trans. Faraday Soc. 58 (1962) 1108–1116
- [40] R.R. Baker, R.R. Baldwin, R.W. Walker, The use of the H₂ + O₂ reaction in determining the velocity constants of elementary reaction in hydrocarbon oxidation, Symp. (Int.) Combust. 13 (1971) 291–299.
- [41] R.A. Yetter, F.L. Dryer, Inhibition of moist carbon monoxide oxidation by trace amounts of hydrocarbons, Symp. (Int.) Combust. 24 (1992) 757–767.
- [42] M.A. Mueller, R.A. Yetter, F.L. Dryer, Measurement of the rate constant for H + O₂ + M → HO₂ + M (M = N₂, Ar) using kinetic modeling of the high-pressure H₂/O₂/NO₂ reaction, Symp. (Int.) Combust. 27 (1998) 177–184.
- [43] R. Song, N.D. DeLuca, M.P. Burke, Towards Autonomous Kinetic Model Improvement through Automated Experiments and Computations, Eastern States Meeting of the Combustion Institute, Princeton, New Jersey, March 2016.
- [44] N. Baker, F. Alexander, T. Bremer, A. Hagberg, Y. Kevrekidis, H. Najm, M. Parashar, A. Patra, J. Sethian, S. Wild, et al., Workshop Report on Basic Research Needs for Scientific Machine Learning: Core Technologies for Artificial Intelligence, Tech. rep., USDOE Office of Science (SC), Washington, DC (United States), 2019.
- [45] S.M. Correa, A review of NO_x formation under gas-turbine combustion conditions, Combust. Sci. Tech. 87 (1993) 329–362.
- [46] A. Durocher, G. Bourque, J.M. Bergthorson, Quantifying the effect of kinetic uncertainties on NO predictions at engine-relevant pressures in premixed methane-air flame, Proc. ASME Turbo Expo (2019) GT2019–90486.
- [47] P. Glarborg, J.S. Allingham, A.B. Skov, H. Hashemi, P. Marshall, Re-examination of the N₂O + O reaction, J. Phys. Chem. A 127 (2023) 6521–6531.
- [48] F. Winter, C. Wartha, H. Hofbauer, NO and N₂O formation during the combustion of wood, straw, malt waste and peat, Bioresource Tech. 70 (1999) 39–49.
- [49] W.R. Anderson, N.E. Meagher, J.A. Vanderhoff, Dark zones of solid propellant flames: Critically assessed datasets, quantitative model comparison, and detailed chemical analysis, Combust. Flame 158 (2011) 1228–1244.
- [50] R.E. Cornell, M.C. Barbet, M.P. Burke, Automated discovery of influential chemically termolecular reactions in energetic material combustion: A case study for RDX, Proc. Combust. Inst. (2021) 787–794.
- [51] P. Glarborg, J.A. Miller, B. Ruscic, S.J. Klippenstein, Modeling nitrogen chemistry in combustion, Prog. Energy Combust. Sci. 67 (2018) 31–68.

- [52] N.E. Meagher, W.R. Anderson, Kinetics of the O(³P) + N₂O reaction: Interpretation and recommended rate coefficients, J. Phys. Chem. A. 104 (2000) 6013–6031.
- [53] J. Lee, M.C. Barbet, C.E. LaGrotta, Q. Meng, F.M. Haas, M.P. Burke, A consistent explanation of seemingly inconsistent experimental and theoretical data for N₂O + O via MultiScale Informatics, Combust. Flame (2023) http://dx.doi.org/10.1016/j.combustflame.2024.113563, In press.
- [54] D.F. Davidson, M.D. DiRosa, A.Y. Chang, R.K. Hanson, Shock tube measurements of the major product channels of N₂O + O, Int. Symp. Shock Waves 18 (1991) 813–818.
- [55] T.V. Pham, T.J. Tsay, M.C. Lin, Thermal decomposition of N₂O near 900 K studied by FTIR spectrometry: Comparison of experimental and theoretical O(³P) formation kinetics, Int. J. Chem Kinet. 52 (2020) 632–644.
- [56] F.M. Haas, F.E. Alam, J.S. Santner, T.I. Farouk, F.L. Dryer, Branching ratio of N₂O + O → Products determined from flow reactor experiments at intermediate temperatures, in: 11th U.S. National Combustion Meeting, 2019.
- [57] R.E. Cornell, M.C. Barbet, M.P. Burke, Toward a more comprehensive understanding of the kinetics of a common biomass-derived impurity: NH_3 oxidation by N_2O in a jet-stirred reactor, Energy Fuels 35 (2021) 13338–13348.
- [58] O. Herbinet, B. Husson, Z. Serinyel, M. Cord, V. Warth, R. Fournet, P.-A. Glaude, B. Sirjean, F. Battin-Leclerc, Z. Wang, M. Xie, Z. Cheng, F. Qi, Experimental and modeling investigation of the low-temperature oxidation of n-heptane, Combust. Flame (2012) 3455–3471.
- [59] O. Herbinet, P.M. Marquaire, F. Battin-Leclerc, R. Fournet, Thermal decomposition of n-Dodecane: Experiments and kinetic modeling, J. Anal. Appl. Pyrolysis 78 (2007) 419–429.
- [60] O. Herbinet, F. Battin-Leclerc, Progress in understanding low-temperature organic compound oxidation using a jet-stirred reactor, Int. J. Chem. Kinet. 46 (2014) 619–639
- [61] D. Matras, J. Villermaux, Un réacteur continu parfaitement agité par jets gazeux pour l'étude cinétique de réactions chimiques rapides, Chem. Eng. Sci. 28 (1973) 129–137.
- [62] R. David, D. Matras, Règies de construction et d'extrapolation des réacteurs auto-agités par jets gazeux, Can. J. Chem. Eng. 53 (1975) 297–300.
- [63] W.W. Ayass, Mixing in jet-stirred reactors with different geometries (Ph.D. thesis), King Abdullah University of Science and Technology, 2013.
- [64] W.W. Ayass, E.F. Nasir, A. Farooq, S.M. Sarathy, Mixing-structure relationship in jet-stirred reactors, Chem. Eng. Res. Design 111 (2016) 461–464.
- [65] R.E. Cornell, M.C. Barbet, J. Lee, M.P. Burke, NH₃ oxidation by NO₂ in a jetstirred reactor: The effect of significant uncertainties in H₂NO kinetics, Appl. Energy Combust. Sci. 12 (2022) 100095.
- [66] J. Lee, M.C. Barbet, Q. Meng, R.E. Cornell, M.P. Burke, Experimental support for a new ${\rm NO_x}$ formation route via an HNNO intermediate, Combust. Flame 257 (2023) 112632.
- [67] P. Azay, G.-M. Côme, Temperature gradients in a continuous flow stirred tank reactor, Indust. Eng. Chem. Proc. Des. Dev. 18 (4) (1979) 754–756.
- [68] C.E. LaGrotta, M.C. Barbet, L. Lei, M.P. Burke, Towards a high-accuracy kinetic database informed by theoretical and experimental data: CH₃ + HO₂ as a case study, Proc. Combust. Inst. 38 (2021) 1043–1051.
- [69] C.E. LaGrotta, Q. Meng, L. Lei, M.C. Barbet, Z. Hong, M.P. Burke, Resolving discrepancies between state-of-the-art theory and experiment for $\rm HO_2 + \rm HO_2$ via multiscale informatics, J. Phys. Chem. A 127 (2023) 799–816.
- [70] M.C. Barbet, Progress Towards Automatic Chemical Kinetic Model Development (Ph.D. thesis), Columbia University, 2023.
- [71] J.E. Johnsson, P. Glarborg, K. Dam-Johansen, Thermal dissociation of nitrous oxide at medium temperatures, Symp. (Int.) Combust. 24 (1992) 917–923.
- [72] F. Kaufman, N.J. Gerri, R.E. Bowman, Role of nitric oxide in the thermal decomposition of nitrous oxide, J. Chem. Phys. 25 (1956) 106–115.
- [73] M. González, R. Valero, R. Sayós, Ab initio ground potential energy surface (3 A") for the O(3 P) + N₂O reaction and kinetics study, J. Chem. Phys. 115 (2001) 2540–2549.
- [74] T.V. Pham, M.C. Lin, Investigation of product formation in the $O(^1D, ^3P) + N_2O$ reactions: Comparison of experimental and theoretical kinetics, J. Phys. Chem. A 126 (2022) 1103–1113.